MS accepted by JQSRT on 9 January 2020 – https://doi.org/10.106/j.jqsrt.2020.106841

Two-photon excitation of two Rydberg levels of O_2 above 95 130 cm^{-1}: rotational-state dependence of predissociation linewidths

Mitsuhiko Kono[a,c], Yabai He[b], Brenton R Lewis[a],
Stephen T Gibson[a], Kenneth G H Baldwin[a] and Brian J Orr[b,*]

a *Research School of Physics, The Australian National University, Canberra, ACT 2601, Australia*
E-mail: mitsu.kono@anu.edu.au, brenton.lewis@anu.edu.au, stephen.gibson@anu.edu.au, kenneth.baldwin@anu.edu.au

b *MQ Photonics Research Centre, Department of Physics and Astronomy, Macquarie University, Sydney, NSW 2109, Australia*
E-mail: brian.orr@mq.edu.au, yabai.he@mq.edu.au, yabaihe@hotmail.com

c Present address: *The Senri International School of Kwansei Gakuin, Osaka 562-0032, Japan*
E-mail: mikono@senri.ed.jp

* Corresponding author. *E-mail adddress:* brian.orr@mq.edu.au (B. Orr)

Single-file MS pages (including embedded figures): 23; References: 39; Figures: 5

ABSTRACT

Two-photon absorption is employed to record sub-Doppler molecular-beam spectra of oxygen ($^{16}O_2$), excited to the $v' = 1$ level of its ($X\,^2\Pi_g$) $5d\pi\ ^1\Sigma_g^+$ Rydberg state above 95 130 cm^{-1} and detected by photoionisation in a time-of-flight instrument. A nonlinear-optical source generates single-longitudinal-mode pulses of coherent ultraviolet light at ~210 nm with sufficiently narrow optical bandwidth to enable more detailed lineshape measurements of rovibronic features than had been achieved in an early investigation [Pratt *et al.*, J. Chem. Phys. 1990; 93: 3072–84]. A spectral width of 0.59 ± 0.02 cm^{-1} is derived by Lorentzian and Beutler-Fano lineshape fits to the prominent $^PQ_{13}(0)$ feature, nominally at ~95 133.7 cm^{-1} in that spectrum; our estimated width is significantly narrower than the previously reported width of ~1.0 cm^{-1}. Likewise, the adjacent $^RQ_{11}(2)$ feature, nominally at ~95 143.8 cm^{-1}, is found to be markedly broader (2.2 ± 1.5 cm^{-1}), which is consistent with the supposed effects of J'-dependent predissociation arising from overlap between the ($X\,^2\Pi_g$) $5d\pi\ ^1\Sigma_g^+$ Rydberg manifold and other dissociative states. The dependence of the O_2^+ and O^+ ion signals on acceleration voltages, O_2-jet stagnation pressure, ultraviolet pulse energy and optical polarisation are also examined.

Keywords:
Oxygen; Rydberg spectra; Lineshapes; Predissociation; Nonlinear-optical light source

1. Introduction

There have long been extensive investigations of the spectroscopy and energetics of molecular oxygen ($^{16}O_2$), which sustains our terrestrial environment and its atmospheric photochemistry. Strong absorption in the $B\,^3\Sigma_u^- \leftarrow X\,^3\Sigma_g^-$ Schumann-Runge (SR) band system at 175–205 nm in the vacuum ultraviolet (UV) is notable. The high-energy $B\,^3\Sigma_u^-$ electronic manifold is widely affected by predissociation, arising from rovibronic interactions with various repulsive electronic states that correlate with two separated ground-state oxygen atoms (O ^3P). Such predissociation effects in O_2 have been of scientific interest for more than eighty years [1,2]. Spectroscopic linewidths associated with predissociation in the $B\,^3\Sigma_u^-$ electronic manifold have therefore attracted much attention with regard to their fine-structure and rotational-state dependencies [3–5]. Other fine-structure-resolved studies of the SR bands have examined collisional self-broadening [6] and lineshape asymmetries due to destructive quantum interference [7–9].

This paper is concerned with rotationally resolved predissociation effects in *gerade*-symmetry Rydberg states of O_2, populated by two-photon excitation (TPE) at rovibronic energies well above the bound states of the $B\,^3\Sigma_u^-$ manifold. Within the same context, the $(X\,^2\Pi_g)$ $ns\sigma_g\,^{1,3}\Pi_g$ Rydberg states of O_2, based on the $(X\,^2\Pi_g)$ O_2^+ core with n = 3, 4 or 5, have been critically re-examined in 1999 [10,11] and experimental observations used to optimise a coupled-channel Schrödinger-equation model. More recently, (2 + 1) resonance-enhanced multiphoton ionisation (REMPI) has been applied [12,13] to velocity-map imaging of O(^3P) and O(^1D) photodissocation fragments generated by TPE of O_2 to the $v' = 0$ and $v' = 1$ vibrational levels of its $(X\,^2\Pi_g)$ $3s\sigma_g\,C\,^3\Pi_g$ Rydberg manifold at UV wavelengths λ_{UV} of 303.5–305.5 nm and 294.5–297.5 nm, respectively. We note also earlier velocity-map photodissocation imaging experiments performed on O_2 with single-photon absorption in the Herzberg continuum region [14,15].

Of particular relevance to the experiments reported in this paper is the work of Pratt *et al.* [16], in which wide-ranging UV TPE spectra were recorded for weakly allowed transitions of form $(X\,^2\Pi_g)$ $(n + 1)s / nd\,^1\Sigma_g^+ (v') \leftarrow X\,^3\Sigma_g^- (v'' = 0)$, where $n > 2$ and the upper vibronic (v') levels are complicated, 'hybridised' $^{1,3}\Pi_g$ Rydberg states [17–19]. The spectra of interest [16] were recorded by REMPI, based on an upconverted pulsed dye laser system which yielded UV TPE spectral features with a uniform full-width-half-maximum (fwhm) of ~1 cm^{-1} (~30 GHz). Our current experiments employ a more elaborate tunable nonlinear-optical system with a

much narrower UV optical bandwidth that is capable of ~20 times higher resolution; this has enabled us to make more highly resolved measurements of the lineshape of individual features in the O_2 Rydberg spectrum and to reveal rotational-state-dependent predissociation processes.

2. Experimental methods

The experimental details described in this section are: the distinctive tunable nonlinear-optical system used to record UV TPE spectra of O_2; the REMPI TOF molecular-beam apparatus; essential instrumental factors in the present UV TPE measurements of O_2 spectra, compared to our previous mass-selective atomic-beam investigations of Xe.

2.1 Tunable UV laser-spectroscopic system

The versatile high-performance laser-based UV spectroscopic system used in our experiments is based on narrowband operation of a pulsed optical parametric oscillator (OPO) that is injection-seeded by a continuous-wave titanium:sapphire (cw Ti:S) ring laser, generating tunable narrowband single-longitudinal-mode (SLM) near-infrared (IR) pulses (at $\lambda_{IR} \approx 840$ nm, with ~25-ns duration and ≤5-μJ energy). This SLM pulsed oscillator stage provides the high peak power and narrow optical bandwidth needed for subsequent multi-stage amplification and nonlinear-optical coherent fourth-harmonic upconversion to mid-UV wavelengths (λ_{UV}) of ~210 nm. Our all-solid-state pulsed UV tunable light source has been used previously for high-resolution atomic spectroscopy, most recently sub-Doppler TPE of xenon (Xe) at 205–213 nm [20,21]. Earlier developmental applications have included studies of krypton (Kr) at ~212.5 nm [22] and cesium (Cs) at ~822.5 nm [23,24]. It has been demonstrated by spectroscopic measurements [20,21] that our pulsed nonlinear-optical system produces tunable coherent SLM UV output at ~210 nm with a TPE-spectroscopic bandwidth $\Delta\nu_{TPE}$ of ~0.006 cm^{-1} (~180 MHz); this is sufficiently narrow for reliable lineshape measurements of individual predissociation-limited features in the O_2 Rydberg spectra of interest. The wavelength λ_{seed} of the cw Ti:S seed laser is monitored by a fiber-coupled wavelength meter (HighFinesse, model WS7; specified accuracy: ± 60 MHz = ± 0.002 cm^{-1}). The OPO cavity is actively locked to λ_{seed}, so that "mode-pulling" of its pulsed output frequency at λ_{IR} is expected to be no more than ~60 MHz (~0.002 cm^{-1}), with relatively little effect on the tolerance of λ_{UV} (= λ_{IR} / 4); the corresponding shift of the two-photon energy ν_{TPE} would be ~0.48 GHz (~0.016 cm^{-1}).

We have used (2 + 1) REMPI for the $5p^5\ 10p\ [5/2]_2$ TPE resonance of Xe (with centroids at $\lambda_{IR} = 840.498$ nm, $\lambda_{UV} = 210.125$ nm and $\nu^0_{TPE} = 95\,181.66$ cm^{-1} [20,21]) to check the frequency calibration of the overall spectroscopic system. This measurement yields $\lambda_{IR} = 840.4964$ nm, $\lambda_{UV} = 210.124$ nm and $\nu^0_{TPE} = 95\,181.85$ cm^{-1}, indicating a discrepancy of ~0.2 cm^{-1} in ν^0_{TPE} for Xe. On this basis, it is likely that our measured scale for two-photon energy ν_{TPE} in our REMPI spectra of O_2 is accurate to ±0.2 cm^{-1} (±6 GHz). We note that the absolute accuracy claimed [16] for ν_{TPE} in previous TPE-spectroscopic measurements of O_2 is no better than ±1 cm^{-1}. The corresponding spectral peak centers from those earlier spectra will be identified by their nominal two-photon energies ν_{TPE}, as previously reported [16].

2.2 Time-of-flight TPE spectrometer

As in our recent experiments on mass-selective TPE spectra of Xe [21], we employ an atomic/molecular-beam apparatus comprising a pulsed supersonic slit-jet valve together with a time-of-flight (TOF) mass spectrometer, adapted from instrumentation originally used [25] for ground-state Lamb-shift studies at ~120 nm of the $1\ ^1S \rightarrow 2\ ^1S$ two-photon transition of helium (He).

Propagating horizontally along the long axis of the vacuum chamber, the pulsed UV beam (with pulse energy typically ~100 μJ at $\lambda_{UV} \approx 210$ nm, usually vertically polarised) crosses the O_2-jet expansion zone with a focused optical beam waist of ~0.1 mm. The horizontally directed ~50-μs free-jet pulse of O_2 gas (BOC industrial grade, >99.5% purity) emanates from the slit aperture (0.5 mm high × 5 mm wide) of a pulsed solenoid valve (General Valve with Iota One driver), with its axis orthogonal to the UV beam. Various stagnation pressures P of neat O_2 gas have been used, but ~100 kPa is found to be optimal. A turbomolecular pump (Pfeiffer model TMU 521 P), mounted directly opposite the pulsed valve, is used to maintain an intra-chamber vacuum of ~3×10^{-5} Pa (~2×10^{-7} Torr) at low stagnation pressures.

The TOF ion-detection system, depicted in **Fig. 1,** is based on the classic Wiley-McLaren design [26]. The repeller plate and primary extraction-grid (EG) electrode define a 12-mm-high photoionisation zone (**1**, with adjustable potential difference V_1 between them). Above that (but not shown explicitly in Fig. 1) is a 25-mm-high acceleration zone (**2**, with adjustable potential difference V_2) beneath a secondary electrode grid held at ground potential. Beyond these two zones is a 90-mm field-free drift zone (**3**, $V_3 = 0$) terminated by a double microchannel-plate (MCP) detector (Del Mar Photonics, model MCP 34-10). The electronic readout unit for the MCP produces a signal output in mV. The vertical TOF axis extends

upwards from the intersection point of the UV and molecular beams, with their common plane 1–2 mm above the repeller plate. The MCP signals are processed digitally and logged together with readings of λ_{IR} (whence $\lambda_{UV} = \lambda_{IR} / 4$) from the wavelength meter and UV photodiode output (I_{UV}, proportional to shot-to-shot UV pulse energy) to generate UV TPE spectra. It is estimated that any Doppler frequency shift due to possible non-orthogonality between the UV beam and the slightly divergent molecular slit-jet beam should be no more than 0.05 cm^{-1}.

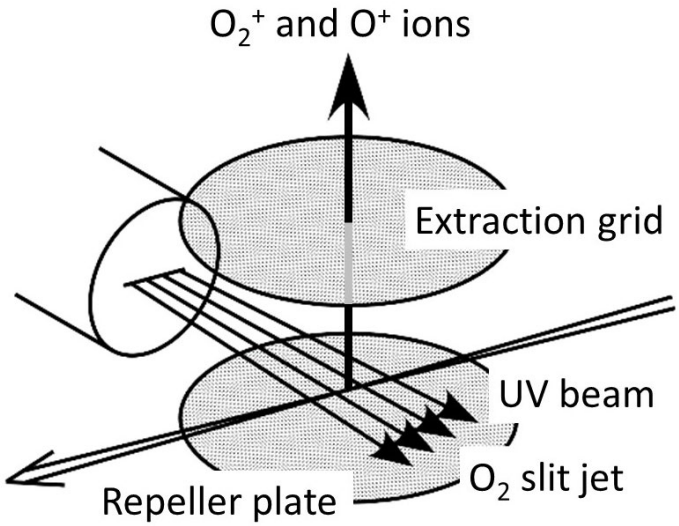

Fig. 1. Schematic diagram of the ionisation zone in the TOF ion-detection system, where the O_2 slit jet and focused UV beam cross 1–2 mm above the repeller plate and 11–10 mm below the extraction grid (with potential difference V_1 between them). Above these (but not depicted here) is a 25-mm acceleration zone (with potential difference V_2) below a grounded secondary electrode grid, a 90-mm field-free drift zone and a microchannel-plate detector to monitor O_2^+ and O^+ ions after they have propagated along the vertical TOF axis.

2.3 Context of these experiments

It is topical at this stage to compare the contrasting degrees of difficulty associated with our current UV TPE measurements of molecular O_2 with those of our previous mass-selective investigations of atomic Xe [21], which were more challenging in terms of the mass resolution required to discern its seven most abundant isotopes and the need to resolve hyperfine structure as well as isotope shifts. On the other hand, our current UV TPE experiments on O_2 entail higher degrees of instrumental difficulty on several fronts:

- As is usual in *molecular* beam experiments, partition-function effects tend to diminish spectroscopically resolved signal strengths relative to those of *atomic* beam experiments.
- Moreover (and most significantly), the "forbidden" singlet–triplet character of the O_2 $(X\,^2\Pi_g)\ 5d\pi\ ^1\Sigma_g^+ \leftarrow X\,^3\Sigma_g^-$ rovibronic transitions studied in the present molecular context

[16] have UV TPE cross sections that are substantially smaller than those that were investigated in our studies of Xe Rydberg states [20,21].

- A further limitation to the signal strength of the rovibronic features of interest in our UV TPE spectra of O_2 is that they are *necessarily* subject to predissociation (*i.e.*, the process that provides the central research theme of this project), causing them to be affected by J'-dependent line broadening and depletion of spectral amplitude. In particular, we note that the O_2 ($X\,^2\Pi_g$) $5d\pi\ ^1\Sigma_g^+ \leftarrow X\,^3\Sigma_g^-$ REMPI spectrum (published in Fig. 6 of [16]) has a substantially lower signal-to-noise ratio (SNR) (with apparently stronger J'-dependent predissociation) than is found in the corresponding (already weak) $4d\pi$ REMPI spectrum in Fig. 5 of [16].
- In view of the above three limitations, the observed signal levels in our current UV TPE-spectroscopic experiments on O_2 are at least an order of magnitude weaker than those experienced in our previous study of Xe [21]; this tends to restrict the modes of electronic detection and signal processing that are available to us.

3. Results and discussion

3.1 Optimisation of O_2^+ and O^+ REMPI TOF signals

Fig. 2 shows REMPI signals in three representative TOF plots **(a)**, **(b)** and **(c)** for a molecular beam of neat O_2 with the ~210-nm UV wavelength λ_{UV} tuned to the peak of the $^PQ_{13}(0)$ rovibronic feature in the (1 – 0) vibrational band of the ($X\,^2\Pi_g$) $5d\pi\ ^1\Sigma_g^+ \leftarrow X\,^3\Sigma_g^-$ system (as shown at a nominal two-photon energy of 95 133.7 cm^{-1} in Fig. 6 of [16]). These plots have been recorded with an O_2-jet stagnation pressure P = 100 kPa (at which SNR is found to be optimal) and the following pairs of acceleration voltages (V_1, V_2): **(a)** (3.0 V, 41.0 V); **(b)** (4.0 V, 40.0 V); **(c)** (5.0 V, 39.0 V). Each TOF plot comprises four characteristic features labelled **A** (at 7.9–8.4 μs), **B** (with an apparent satellite **B'**, at ~10 μs), **C** (at 12.4–13.6 μs) and **D** (broad, at ~14–15 μs). The spectroscopic resonances in REMPI measurements mean that all four features are associated with UV-TPE selection of O_2 ($5d\pi\ ^1\Sigma_g^+$) molecules.

The characteristic UV TPE signals that are most useful for REMPI spectroscopy are the TOF features **A** and **C** in Fig. 2. On the basis of their dependence on the voltages V_1 and V_2 they are attributed to the ions $^{16}O^+$ and $^{16}O_2^+$, respectively. In previous TPE-spectroscopic studies of O_2 Rydberg states [16,18], it was found that *either* O^+ *or* O_2^+ ion signals could be used for REMPI detection, but that the latter was generally more favorable.

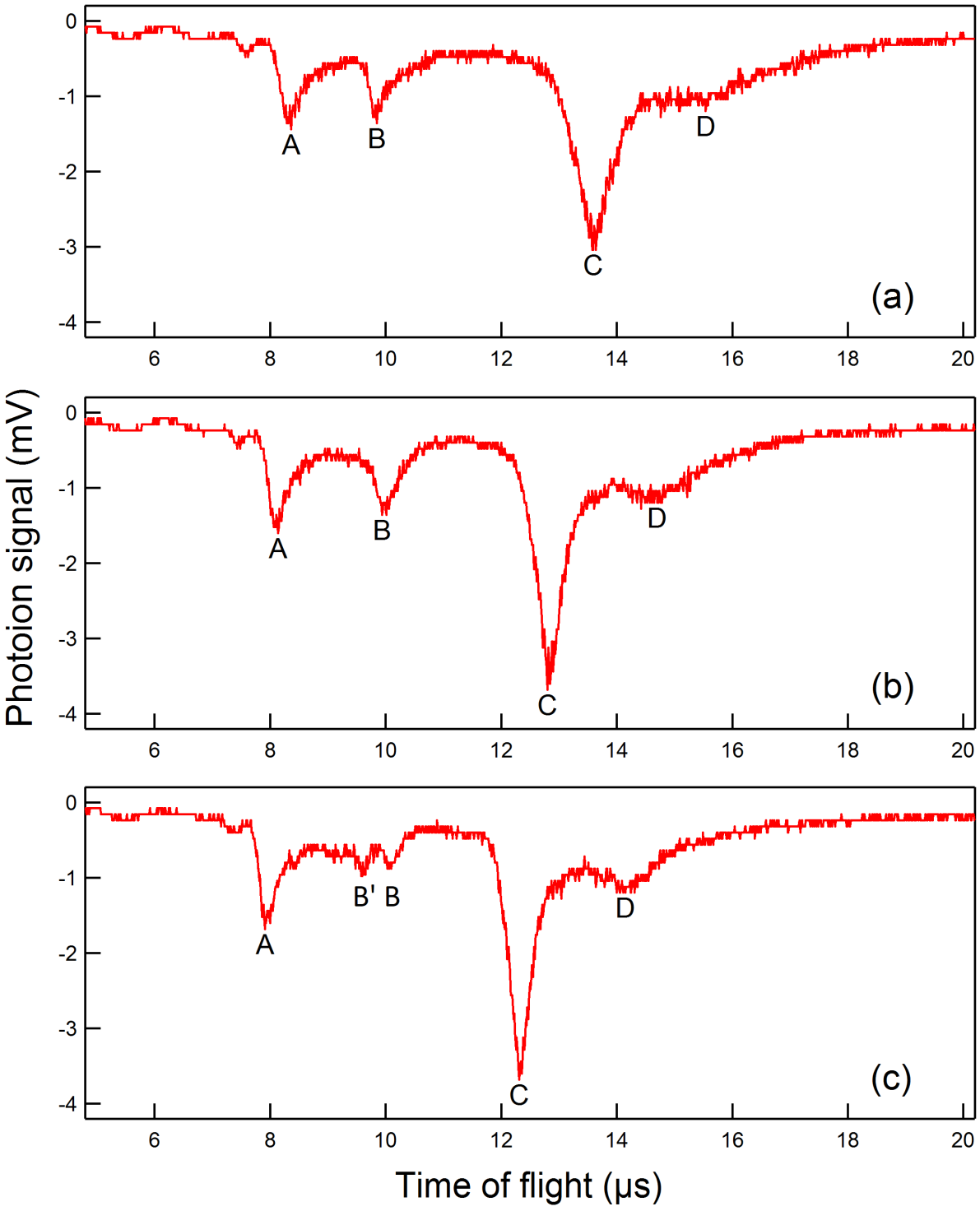

Fig. 2. Representative TOF plots for REMPI of O_2 with the UV TPE wavelength λ_{UV} at ~210 nm tuned to the peak of the $^{P}Q_{13}(0)$ rovibronic feature in the (1 – 0) band of the $(X^2\Pi_g)\ 5d\pi\ ^1\Sigma_g^+ \leftarrow X^3\Sigma_g^-$ system. The plots have been recorded with an O_2-jet stagnation pressure P of 100 kPa and different pairs of acceleration voltages (V_1, V_2) – all with $(V_1 + V_2) = 44.0$ V as specified in Sec. 3.1. Each plot of REMPI photoion signal (mV) against TOF (μs) comprises characteristic features labelled **A**, **B** (with a "satellite" **B'**), **C** and **D**, as discussed in Sec. 3.1.

A kinematic analysis, consistent with formulae in [26] and taking account of the kinetic-energy release (KER) for specific mechanistic steps, agrees well with the observed (V_1, V_2)-dependence of the features **A** (O^+) and **C** (O_2^+) in a range of measured TOF scans, such as those in Fig. 2.

It is evident that (2 + 1) REMPI with $\lambda_{UV} \approx 210$ nm (for which the corresponding single-photon energy is $h\nu \approx 5.90$ eV) can generate O_2^+ TOF signals consistent with either of the following two possible single-photon ionisation steps after promotion of O_2 by TPE to its $5d\pi\ ^1\Sigma_g^+$ Rydberg state [16,27–29]:

$$O_2\ (5d\pi\ ^1\Sigma_g^+) + h\nu \rightarrow O_2^+\ (X\ ^2\Pi_g) + e^- + (\mathrm{KER} = 5.62\ \mathrm{eV}), \quad (1)$$

$$O_2\ (5d\pi\ ^1\Sigma_g^+) + h\nu \rightarrow O_2^+\ (A\ ^2\Pi_u) + e^- + (\mathrm{KER} = 0.65\ \mathrm{eV}). \quad (2)$$

It is also possible that (2 + 1) REMPI at ~210 nm could produce O_2^+ ($a\ ^4\Pi_u$), as follows:

$$O_2\ (5d\pi\ ^1\Sigma_g^+) + h\nu \rightarrow O_2^+\ (a\ ^4\Pi_u) + e^- + (\mathrm{KER} \approx 1.53\ \mathrm{eV}). \quad (3)$$

However, this path to quartet states of O_2^+ is tentative because it would be dependent on the strength of singlet-triplet mixing by spin-orbit coupling within the $5d\pi\ ^1\Sigma_g^+$ Rydberg state.

Production of O^+ ions requires more energy than is provided by (2 + 1) REMPI, so that TOF feature **A** in Fig. 2 entails a further 210-nm UV excitation step, *i.e.*, by (2 + 1 + 1) REMPI:

$$O_2^+\ (A\ ^2\Pi_u) + h\nu \rightarrow O\ (^3P) + O^+\ (^2D) + (\mathrm{KER} = 0.88\ \mathrm{eV}). \quad (4)$$

This final step requires 5.02-eV [27–29] to photodissociate O_2^+ ($A\ ^2\Pi_u$), after its formation as in Eq. (2), into O and O^+ sharing a total KER of 0.88 eV with kinematics corresponding to the TOF feature **A** in Fig. 2. Such a mechanism was previously considered by Park *et al.* [18].

In addition to their dependence on acceleration voltages V_1 and V_2, the observed REMPI TOF signals have been characterised with regard to several other key instrumental factors: stagnation pressure P of neat O_2 supplied to the pulsed valve; direction of linear polarisation of the UV light; UV pulse energy, proportional to photodiode signal I_{UV}. These help assign less regular features **B**, **B'** and **D**, as briefly identified below and further addressed in the Appendix.

Compared to features **A** and **C**, the TOF feature **D** is less useful for REMPI spectroscopy, because the P-dependence of its TOF profile indicates that the flight time of O_2^+ ions is broadened by their non-reactive collisions with residual O_2 gas in the vacuum chamber.

As is explained in the Appendix, the most likely mechanism for the irregular TOF feature **B**, which has a $(I_{UV})^2$ dependence on UV pulse energy and is insensitive to V_1, is understood to entail rapid (lifetime $\tau < 10$ ps) predissociation of O_2 ($5d\pi\ ^1\Sigma_g^+$) Rydberg molecules. Resulting O atoms, with well-defined kinetic energy, then undergo UV-independent ionisation to O^+ later

in their trajectory towards the MCP detector, without any V_1-dependent acceleration (*i.e.*, not until they have reached the extraction grid EG, as portrayed in Fig. 1).

The Appendix also explains the supposed mechanism for another peak, labelled **B'**, that appears to branch out from peak **B** towards lower TOF values when $V_1 \geq 4.5$ V, as in Fig. 2(c). Feature **B'** is shown to arise from O^+ ions that initially propagate backwards and are then electrostatically reflected before they collide with the repeller plate, so that they then propagate towards the MCP detector; this is effectively a delayed, "turned-back" partner of feature **A**.

3.2 High-resolution lineshape measurements in predissociated UV TPE spectra of O_2

Having optimised conditions for REMPI measurements of UV TPE spectra of high-energy predissociated Rydberg states of O_2, we now turn to the spectra of interest themselves. For the (1 – 0) vibrational band of the ($X\,^2\Pi_g$, $\Omega^+ = 3/2$) $5d\pi\ ^1\Sigma_g^+ \leftarrow X\,^3\Sigma_g^-$ system, measured as a UV TPE spectrum with $\lambda_{UV} \approx 210$ nm (as in Fig. 6 of [16]), the most prominent feature in that spectrum is designated $^PQ_{13}(0)$, using the notation $^{\{\Delta N\}}\{\Delta J\}_{F'F''}(J'')$, where, for instance, $\{\Delta J\}$ is "Q" if $J' = J''$, the superscript $\{\Delta N\}$ is "P" if $N' = (N'' - 1)$, and the subscripts F' and F'' designate upper- and lower-state fine-structure components (*e.g.*, "1, 2 or 3" for F_1, F_2 or F_3 in triplet states). Here, in the Hund's case-(b) representation [30], N is the nuclear rotational quantum number with angular momenta related by $\boldsymbol{N} = (\boldsymbol{J} - \boldsymbol{S})$, where electron-spin quantum numbers are $S'' = 1$ and $S' = 0$. This unblended $^PQ_{13}(0)$ line, at a nominal two-photon energy $\nu_{TPE} = 95\,133.7$ cm^{-1} [16], arises through a rovibronic transition, with $J' = J'' = N' = 0$ and $N'' = 1$ from the F_3 fine-structure component of the $v'' = 0$, $X\,^3\Sigma_g^-$ lower level of O_2 up to its F_1, $v' = 1$, $\Omega^+ = 3/2$ ion-core spin-orbit component of the 6*s*/5*d* Rydberg complex. We have also examined the relatively weak $5d\pi\ ^RQ_{11}(2)$ feature in the same UV TPE spectrum of O_2 at a nominal two-photon energy ν_{TPE} of 95 143.8 cm^{-1} (as estimated from Fig. 6 of [16]). This $5d\pi\ ^RQ_{11}(2)$ rovibronic transition has $J' = J'' = N' = 2$ and $N'' = 1$ with F_1 fine structure.

The prominent $5d\pi\ ^PQ_{13}(0)$ feature has been re-measured at higher resolution, as shown in **Fig. 3**. The spectral lineshape has been recorded by step-tuning the wavelength λ_{UV} of our optical UV source [20,21], with its TPE-spectroscopic bandwidth $\Delta\nu_{TPE}$ of ~0.006 cm^{-1}, to successive stable SLM settings of ν_{TPE}. At each of these ν_{TPE} settings, a REMPI-signal data point, shown in arbitrary units (a.u.), has been recorded as the average of 128 UV-laser shots. The TOF detection system has been gated to record O_2^+ signals corresponding to peak **C** in Fig. 2. Each data point has been normalised to the third power of the pulsed UV photodiode output I_{UV}, to correct for point-to-point variations in UV power. The wavelength meter has

been used to log the seed-laser wavelength λ_{seed} (which falls within ±0.002 cm^{-1} of λ_{IR}); ν_{TPE} is then related precisely to λ_{IR} *via* its corresponding wavelength λ_{UV} / 2 (= λ_{IR} / 8). The abscissa of Fig. 3 is thus based on measurements by our wavelength meter. The error bars for each data point denote the scatter of individual UV TPE signal readings; these have been used to weight the lineshape fits appropriately. Also, residuals (Res.) are plotted on a different scale.

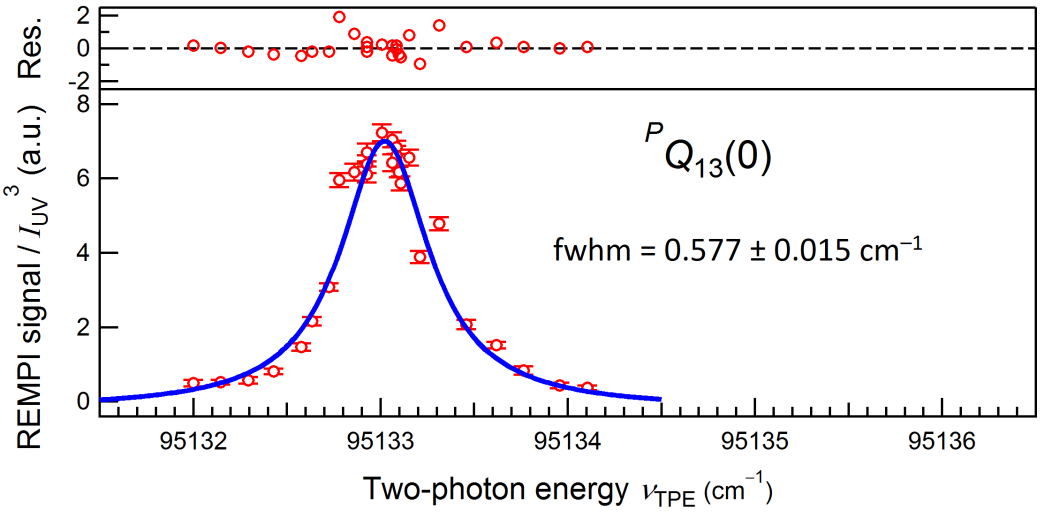

Fig. 3. Lorentzian fit to the prominent $^PQ_{13}(0)$ rovibronic feature in the (1 – 0) band of the ($X\,^2\Pi_g$, $\Omega^+ = 3/2$) $5d\pi\ ^1\Sigma_g^+ \leftarrow X\,^3\Sigma_g^-$ UV TPE spectrum of O_2. Each REMPI-signal data point is the average of 128 UV laser shots, normalised to the third power of the pulsed UV photodiode output I_{UV}, with a stable SLM setting of two-photon energy ν_{TPE} and effective TPE-spectroscopic bandwidth $\Delta\nu_{TPE} \approx 0.006$ cm^{-1}. The Lorentzian fit to this $J' = 0$ feature, nominally at 95 133.7-cm^{-1} [16], has a peak two-photon energy $\nu^0_{TPE} = 95\,133.022 \pm 0.004$ cm^{-1} and fwhm = 0.577 ± 0.015 cm^{-1}, as discussed in Sec. 3.2.

A second set of UV TPE lineshape measurements has been made for the same prominent $^PQ_{13}(0)$ rovibronic feature as shown in Fig. 3. These were performed independently on a separate day, at a stage when normalisation to I_{UV}^3 had not been implemented. The residuals for a Lorentzian fit suggested that this $J' = 0$ feature is slightly asymmetric and that, with its extensive wings, it would be realistic to make a Beutler-Fano fit [31], as in **Fig. 4**. Mechanistic implications of lineshape asymmetry, as *per* the Fano parameter q, are discussed in Sec. 3.3.

Various other lineshape fits for this $J' = 0$ $5d\pi\ ^PQ_{13}(0)$ UV TPE feature have been made to the data plotted in Figs 3 and 4, using either Lorentzian or Beutler-Fano shapes with and without an adjustable non-interacting background term. Not surprisingly, the Beutler-Fano fits, with their increased degrees of freedom, yield reduced residuals compared to simple Lorentzian fits. The fits shown in Figs 3 and 4 have values of peak two-photon energy ν^0_{TPE} differing by ~0.06 cm^{-1}, with fwhm values that are in close agreement. On this basis, our best estimates of

fit parameters (including the ±0.2-cm^{-1} systematic uncertainty in our ν_{TPE} calibration and combining ν^0_{TPE} and fwhm estimates from Figs 3 and 4) are: ν^0_{TPE} = 95 133.0 ± 0.2 cm^{-1}, fwhm = 0.59 ± 0.02 cm^{-1} and (from Fig. 4 alone) q = 10 ± 1. The measured value of ν^0_{TPE} for this 5$d\pi$ $^PQ_{13}(0)$ feature is ~0.7 cm^{-1} less than previously reported (95 133.7 ± 1 cm^{-1}) [16].

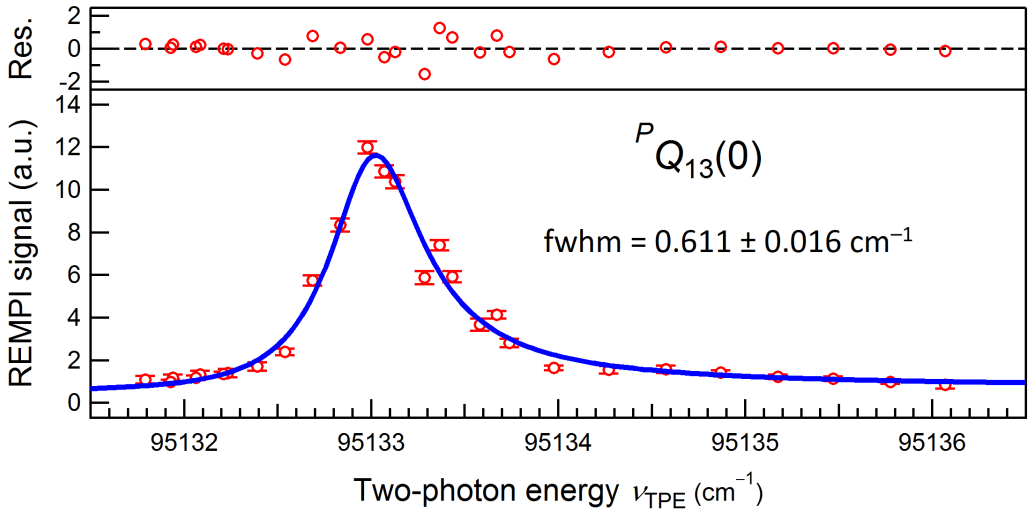

Fig. 4. A second lineshape measurement of the same prominent $^PQ_{13}(0)$ rovibronic feature as in Fig. 3, in the (1 – 0) band of the ($X\,^2\Pi_g$, $\Omega^+ = 3/2$) 5$d\pi$ $^1\Sigma_g^+ \leftarrow X\,^3\Sigma_g^-$ UV TPE spectrum of O_2. Experimental conditions are similar to those in Fig. 3, except that the data points have not been normalised to $I_{UV}{}^3$. The wings of this slightly asymmetric $J' = 0$ feature are sufficiently extensive to allow a Beutler-Fano fit [31] to be made; this fit yields a resonance energy of 95 132.993 ± 0.008 cm^{-1} and a fwhm of 0.611 ± 0.016 cm^{-1}, with Fano parameter q = 10 ± 1.

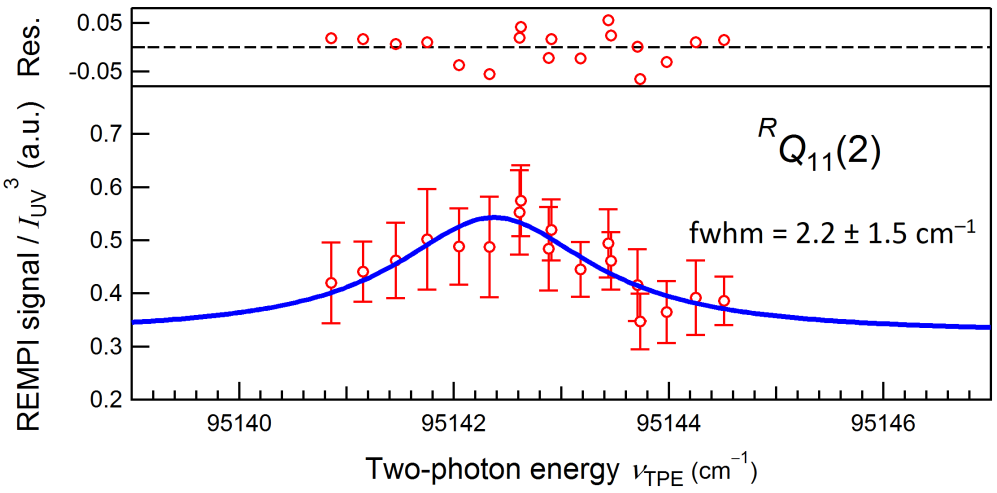

Fig. 5. Lorentzian fit to the relatively weak $^RQ_{11}(2)$ rovibronic feature in the (1 – 0) band of the ($X\,^2\Pi_g$, $\Omega^+ = 3/2$) 5$d\pi$ $^1\Sigma_g^+ \leftarrow X\,^3\Sigma_g^-$ UV TPE spectrum of O_2. Each REMPI-signal data point has been recorded as in the context of Fig. 3. The Lorentzian fit to this $J' = 2$ feature has fwhm = 2.2 ± 1.5 cm^{-1} – significantly broader than for the $J' = 0$ feature observed in Figs 3 and 4.

Lineshape measurements, as portrayed in **Fig. 5**, have also been made for the relatively weak $5d\pi\ ^{R}Q_{11}(2)$ rovibronic feature in the same UV TPE spectrum of O_2 [16]. The Lorentzian fit to this feature has $\nu^0_{TPE} = 95\,142.4 \pm 0.2$ cm^{-1}, which is ~1.4 cm^{-1} smaller than the nominal peak ν_{TPE} value of $95\,143.8 \pm 1$ cm^{-1} (as estimated from Fig. 6 of [16]). The I_{UV}-normalised plots in Figs 3 and 5 have similar noise levels, but the peak signal amplitude is ~24 times less in the case of Fig. 5 – insufficient to allow a reliable Beutler-Fano fit. It is significant (in terms of predissociation effects, as will be discussed in Sec. 3.3) that the ~2.2-cm^{-1} fwhm of this $J' = 2$ feature is ~3.7 times broader than that of the $J' = 0$ feature (as observed in Figs 3 and 4).

3.3 Interpretation of spectroscopic results for predissociated Rydberg levels of O_2

At the outset, we note three significant aspects of the previously reported spectroscopic measurements [16] which have been re-visited in Sec. 3.2 above, as follows:

- *Simulations of previous UV TPE spectra.* Using spectroscopic constants from [16], the spectroscopic simulation program PGOPHER [32] provides an excellent fit to two-photon energies ν_{TPE} for the (1 – 0) band of the $(X\,^2\Pi_g,\ \Omega^+ = 3/2)\ 5d\pi\ ^1\Sigma_g^+ \leftarrow X\,^3\Sigma_g^-$ TPE spectrum of O_2, as shown in Fig. 6 of [16]. As expected, PGOPHER indicates that the $^{P}Q_{13}(J'')$ sub-band arises from the T_0^0 spherical-tensor component of the TPE transition moment, that the $^{R}Q_{11}(J'')$ sub-band (with $J'' \geq 2$) has contributions from both T_0^0 and T_0^2, and that the $^{P}O_{11}(J'')$ and $^{R}S_{13}(J'')$ sub-bands are associated with T_0^2. However, the peak amplitudes observed in $(X\,^2\Pi_g,\ \Omega^+ = 3/2)\ nd\pi\ ^1\Sigma_g^+ \leftarrow X\,^3\Sigma_g^-$ TPE spectra of O_2 (with n = 4–6) [16] TPE spectra [16] do not match relative line strengths predicted by the basic version of the PGOPHER program [32] with any realistic choice of effective rotational temperature T_{rot} and the ratio T_0^0 / T_0^2 of TPE transition-moment contributions. If more extensive observed data were available, PGOPHER might then be adapted to simulate the spectral amplitudes by allowing empirically for J'-dependent predissociation effects.
- *J'-dependence of rovibronic line strengths in previous UV TPE spectra.* We note that Fig. 6 of [16] shows a pronounced depletion of TPE line strength as J' increases within the (1 – 0) band of the $(X\,^2\Pi_g,\ \Omega^+ = 3/2)\ 5d\pi\ ^1\Sigma_g^+ \leftarrow X\,^3\Sigma_g^-$ TPE spectrum of O_2. The relative peak heights for three characteristic features are: $^{P}Q_{13}(0) : {}^{R}Q_{11}(2) : {}^{R}Q_{11}(4) = 1.0 : 0.19 : 0.03$; the first two entries agree with our measured ratio of $1.0 : 0.15 \pm 0.05$ for our REMPI signal strengths, normalised to I_{UV} and profile-integrated, in Figs 3 and 5. However, such apparent relative line strengths are far from what can be predicted

realistically simply by varying T_{rot} and the T_0^0 / T_0^2 ratio. Meanwhile, the (1 – 0) band of the ($X\,^2\Pi_g$, $\Omega^+ = 3/2$) $4d\pi\ ^1\Sigma_g^+ \leftarrow X\,^3\Sigma_g^-$ TPE spectrum of O_2, as in Fig. 5 of [16], shows a much less pronounced J'-dependent depletion of line strength; the corresponding relative peak heights are 1.0 : 0.57 : 0.03. These trends are attributed to a much greater J'-dependence of predissociation-induced depletion of observed rovibronic line strengths for the Rydberg state at the higher energy ($5d\pi$) than at the lower energy ($4d\pi$). This appears to contravene the usual trend, in Rydberg manifolds that are less markedly affected by J'-dependent predissociation, that linewidths vary as $(n^*)^{-3}$, where n^* is the effective principal quantum number (including a quantum defect $\delta = n - n^*$).

- *Linewidths in previous UV TPE spectra.* Observed spectroscopic fwhm values have been estimated for features in the UV TPE spectra that were reported for $v' = 1$ levels of the ($X\,^2\Pi_g$, $\Omega^+ = 3/2$) $nd\pi\ ^1\Sigma_g^+$ Rydberg states of O_2 with principal quantum number $n = 4$, 5 and 6, as in Figs 5–7 of [16]. Those figures would probably have been traced by a draughtsman before publication. Nevertheless, we deduce that each $nd\pi$ spectrum has a uniform fwhm which is apparently independent of spectroscopic feature or the value of J'. Within the $\Omega^+ = 3/2$ ion-core spin-orbit component of the $(n+1)s\,/\,nd$ Rydberg complexes, fwhm values vary with values of n as follows: for $n = 4$, ~0.7 cm^{-1}; for $n = 5$ 4, ~1.0 cm^{-1}; for $n = 6$, ~1.5 cm^{-1}. This trend in fwhm values indicates a steady increase in predissociation-induced broadening for each $nd\pi$ Rydberg state with increasing n. Such a trend, in which predissociation linewidths increase with n (and $n^* \approx n + 0.06$ [16]), is again contrary to the $(n^*)^{-3}$ rule that is often found [10] in less markedly predissociated Rydberg manifolds. The early experiments [16] employed an upconverted dye laser based on a design [33] that would, at best, have resulted in SLM optical bandwidths of ~0.02 cm^{-1} at ~630 nm and (after third-harmonic generation) ~0.06 cm^{-1} at ~210 nm; the resulting TPE-spectroscopic bandwidth $\Delta\nu_{TPE}$ would therefore have been at least 0.12 cm^{-1} (and probably more than that, depending on how readily the upconverted dye laser could be tuned continuously without mode hops).

Our high-resolution UV TPE lineshape measurements have extended the above three aspects of the previous wide-ranging spectroscopic study [16]. As explained in Sec. 2.1, the wavelength meter can be used to calibrate the scale of two-photon energy ν_{TPE} *via* (2 + 1) REMPI TOF spectra of Xe; this yields a likely systematic uncertainty of ±0.2 cm^{-1}. On that scale, the $5d\pi\ ^PQ_{13}(0)$ and $5d\pi\ ^RQ_{11}(2)$ peaks in Figs 3 and 5 have been measured respectively to be at 95 133.0 cm^{-1} and 95 142.4 cm^{-1}, each with the above systematic uncertainty of ±0.2

cm^{-1}. These are respectively ~0.7 cm^{-1} and ~1.4 cm^{-1} smaller than the corresponding nominal values of peak two-photon energies ν^0_{TPE} of 95 133.7 ± 1 cm^{-1} and 95 143.8 ± 1 cm^{-1}, as estimated from Fig. 6 of [16]. Our Figs 3–5 have linear ν_{TPE} scales spanning a few cm^{-1} around each spectral peak; these are derived from the wavelength meter, which is specified to be highly accurate (±0.002 cm^{-1}). Moreover, as already mentioned in Sec. 2.2, any Doppler shift, arising from non-orthogonal crossing of the UV and molecular beams, should be small (≤0.05 cm^{-1}).

The above discrepancy of –0.7 cm^{-1}, between our measurements of the peak ν_{TPE} value for the ${}^{P}Q_{13}(0)$ feature and that in [16], is best regarded as a systematic difference that is within the ±1-cm^{-1} absolute uncertainty of those previous measurements. However, the larger discrepancy of –1.4 cm^{-1}, between present and past measurements of the peak ν_{TPE} value for the ${}^{R}Q_{11}(2)$ feature, deserves more serious consideration as it seems to add a further discrepancy of –0.7 ± 0.2 cm^{-1}. A hypothetical explanation of this discrepancy (at least in part) could be that, in recording the spectrum portrayed in Fig. 6 of [16], there might have been an unrecognised discontinuity or irregularity of ~0.2 cm^{-1} in the dye-laser wavelength scan between ν_{TPE} values of 95 134 cm^{-1} and 95 142 cm^{-1}. Such a change in the separation between the ${}^{P}Q_{13}(0)$ and ${}^{R}Q_{11}(2)$ peaks would then have affected the value of the upper-state rotational constant B', which can be estimated from the upper-state rotational term energy $B'\,J'\,(J'+1)$. For the ${}^{P}Q_{13}(0)$ transition, this term energy is independent of B', since $J' = N' = 0$; however, it equals 6 B' for the ${}^{R}Q_{11}(2)$ transition where $J' = N' = 2$. According to our hypothesis, B' would therefore change by approximately (–0.2 cm^{-1}) / 6 and therefore shift from 1.814 cm^{-1} [16] to ~1.78 cm^{-1}. This would yield a value of $B'(v' = 1)$ that is more plausible in terms of conventional anharmonic-oscillator trends, with values of B' for $v' = 0$, 1 and 3 becoming 1.80, 1.78 and 1.73 cm^{-1}, respectively; this would effectively eliminate the previous $v' = 1$ outlier of 1.814 cm^{-1} as in Table II of [16]. Although our hypothetical proposition is somewhat speculative, it does offer reconciliation of apparent anomalies, accounting for a portion (but not all!) of our unexpected ν_{TPE}-calibration discrepancies and tentatively explaining the previous irregularity of $B'(v' = 1)$ for O_2 in its $nd\pi\ {}^{1}\Sigma_g^+$ Rydberg manifold [16].

The absolute calibration of ν_{TPE} should not detract from our principal results, concerning the apparent effect of J'-dependent predissociation-lifetime broadening on fwhm values from high-resolution lineshape measurements for the $5d\pi\ {}^{P}Q_{13}(0)$ and $5d\pi\ {}^{R}Q_{11}(2)$ UV TPE features (as in Figs 3–5). This is facilitated (as explained in Sec. 2.1) by the narrow TPE-spectroscopic bandwidth provided by our nonlinear-optical system [20,21] which generates SLM pulses of coherent UV light at ~210 nm and offers a 20-fold enhancement of spectral resolution relative

to previous experiments [16]. This effective spectroscopic bandwidth $\Delta\nu_{TPE}$ is sufficiently narrow to enable our detailed lineshape measurements for the rovibronic features of interest.

In particular, lineshape fits (as in Figs 3 and 4) indicate that the prominent $5d\pi\ ^{P}Q_{13}(0)$ peak has a fwhm of 0.59 ± 0.02 cm^{-1} (significantly narrower than the previously reported fwhm of ~1.0 cm^{-1} [16]); the corresponding predissociation lifetime is $\tau = 8.9 \pm 0.3$ ps. On the other hand, the adjacent, weaker $5d\pi\ ^{R}Q_{11}(2)$ feature has a markedly broader fwhm (2.2 ± 1.5 cm^{-1}, corresponding to $\tau \approx 2.4$ ps). Whereas there was no indication of such J'-dependent variations in fwhm from the earlier work [16], our lineshape fits suggest that J'-dependent predissociation-lifetime broadening causes the relatively weak $5d\pi\ ^{R}Q_{11}(2)$ feature with $J' = 2$ (as in Fig. 5) to be about four times broader than the prominent $5d\pi\ ^{P}Q_{13}(0)$ feature with $J' = 0$ (as in Figs 3 and 4). This contrast may be understood simply in terms of the fact that Rydberg levels with $J' > 0$ in the ($X\,^2\Pi_g$, $\Omega^+ = 3/2$) $5d\pi\ ^1\Sigma_g^+$ Rydberg manifold have access to a wider range of predissociative coupling channels (*e.g.*, involving interactions with dissociative valence states [10,11,34]) than the level with $J' = 0$.

More explicitly, the level with $J' = 0$ in the $5d\pi\ ^1\Sigma_g^+$ Rydberg manifold can be coupled directly only by spin-orbit interaction to any $^3\Pi_g$ ($\Omega = 0$) or $^3\Sigma_g^-$ states that happen to overlap it. The 1999 survey by Morrill *et al.* [10] indicates that linewidths for ($X\,^2\Pi_g$) $ns\sigma_g\ ^3\Pi_g$ Rydberg states with $n > 5$ are unlikely to contribute as much as the ~0.6 cm^{-1} of predissociation width that is observed in Figs 3 and 4. Indirect contributions by as-yet unobserved ($X\,^2\Pi_g$) $nd\ ^3\Pi_g$ Rydberg states, *via* Rydberg-valence coupling to $^3\Pi_g$ dissociative states, are considered more likely sources of the observed predissociation width. On the other hand, ($X\,^2\Pi_g$, $\Omega^+ = 3/2$) $5d\pi\ ^1\Sigma_g^+$ Rydberg levels with $J' > 0$ are amenable to additional coupling channels, including strong rotational interactions with the $^1\Pi_g$ complex members, providing a possible predissociation channel through the subsequent $^1\Pi_g$ Rydberg-valence interactions involving dissociative states. Moreover, the $^1\Sigma_g^+$ manifold can couple strongly with the $^3\Sigma_g^-$ manifold, which is also rotationally coupled to the $^3\Pi_g$ manifold, leading to a less direct predissociation channel *via* the $^3\Pi_g$ Rydberg-valence interactions. Any of these interactions are likely [10,11,34] to provide a mechanism for the $5d\pi\ ^{R}Q_{11}(2)$ $J' = 2$ feature (as in Fig. 4) to be substantially broader than the $5d\pi\ ^{P}Q_{13}(0)$ $J' = 0$ feature (as in Fig. 3).

It should be noted that asymmetric lineshapes are not at all exceptional in spectra that are affected by predissociation, where Beutler-Fano lineshape effects [31,35,36] can arise within a superposition of interfering quantum states, such as a discrete level and an overlapping

continuum. For instance, such effects have been observed in SR bands of O_2 at lower excitation energies [7–9]. Nevertheless, the present instance of lineshape asymmetry for an isolated J'-resolved Rydberg rovibronic level of O_2 is noteworthy. The extensive wings of the UV REMPI data plotted in Fig. 4 reveal an asymmetric lineshape, for which the Fano parameter q is estimated to be 10 ± 1. The fitted Beutler-Fano profile is believed to arise from interaction between the discrete $J' = 0$ $^1\Sigma_g^+$ level and the quasicontinuum associated with the broad wings of the likely resonant interaction that causes predissociation *via* the $^3\Pi_g$ valence manifold.

In addition to the central theme of exploring J'-dependent predissociation linewidths in a high-energy Rydberg rovibronic manifold, our REMPI experiments reveal two irregular TOF processes, of which TOF-plot dependences on (V_1, V_2), UV pulse energy and UV polarisation have been considered in more detail in the Appendix, as follows:

- *UV-independent predissociation and ionisation effects.* The tentatively proposed mechanism for the V_1-independent, $(I_{UV})^2$-dependent feature **B** in Fig. 2 is *not* that of a conventional REMPI process. It is understood to entail detection of O^+ ions formed, without photoionisation or V_1-dependent acceleration in zone **1**, from O atoms arising *via* rapid (< 10 ps) predissociation of TPE-generated O_2 ($5d\pi$ $^1\Sigma_g^+$), with possible schemes as in Eqs (A1)–(A5). We note that, although there are many instances of O_2 predissociation studies in which O atoms are actively probed (*e.g.*, by REMPI in velocity-map imaging experiments [14,15,37,38]), there are fewer cases where atoms from predissociation of UV-excited O_2 are detected quasi-spontaneously (*e.g.*, by luminescence from O (^1D) atoms produced by SR-band photodissociation [39]). It could be informative to use velocity-map imaging to further examine the processes that have yielded feature **B**.

- *Reflection of backward-ejected O^+ ions.* TOF values for the peak **B'** that appears in Fig. 2(c) – but not at lower values of V_1 in Figs 2(a) and (b) – are well modeled in terms of O^+ ions formed by (2 + 1 + 1) REMPI as in the sequence of Eqs (2) and (4) and initially ejected backwards. If $V_1 \geq 4.5$ V, these anisotropically distributed O^+ ions are electrostatically reflected towards the MCP, thereby avoiding destruction by impact with the repeller plate.

4. Concluding remarks

This work is primarily concerned with high-resolution measurements of the ($X^2\Pi_g$, $\Omega^+ = 3/2$) $5d\pi$ $^1\Sigma_g^+ \leftarrow X^3\Sigma_g^-$ UV TPE Rydberg spectrum of O_2, with particular regard to J'-

dependent predissociation-lifetime broadening in the ($v' = 1$, $J' = 0$ and 2) upper levels, determined from Lorentzian fits to lineshapes for the ${}^{P}Q_{13}(0)$ and ${}^{R}Q_{11}(2)$ features, as well as a Beutler-Fano fit to the asymmetric lineshape for the ${}^{P}Q_{13}(0)$ feature. In that spectrum, we have measured those features to be at peak two-photon energies ν^0_{TPE} of 95 133.0 cm^{-1} for ${}^{P}Q_{13}(0)$ and 95 142.4 cm^{-1} for ${}^{R}Q_{11}(2)$. Comparison with a previous spectroscopic study [16] reveals assorted mechanistic trends, not all consistent with our current observations. It is particularly significant that the $J' = 0$ Rydberg level is observed to have a fwhm of 0.59 ± 0.02 cm^{-1}, which is 3.7 ± 2.5 times narrower (and hence has a longer predissociation lifetime) than for the $J' = 2$ Rydberg level (which is more amenable to coupling with overlapping dissociative states). Additional insight into the accompanying photo-excitation and ionisation processes has been gained by systematically studying and modeling the dependence of observed REMPI TOF signals on various experimental conditions.

Appendix

Observed REMPI TOF signals of the form shown in Fig. 2 have, as already outlined in Sec. 3.1, been characterised systematically with regard to several key instrumental factors: acceleration voltages V_1 and V_2; stagnation pressure P of neat O_2 supplied to the pulsed valve; direction of linear polarisation of the UV light; UV pulse energy (proportional to photodiode output I_{UV}). Kinematic analysis of the (V_1, V_2)-dependence of features **A** and **C** in Fig. 2 suffices to assign them to the ions ${}^{16}O^+$ *via* (2 + 1 + 1) REMPI and ${}^{16}O_2^+$ *via* (2 + 1) REMPI, respectively, as in the context of Eqs (1)–(4). However, additional key instrumental factors are required for mechanistic characterisation of the less regular features **B**, **B'** and **D** in Fig. 2.

As already mentioned in Sec. 3.2, the relatively broad TOF feature **D** has a P-dependence consistent with collisional broadening of TPE-selected O_2^+-ion signals by residual O_2 gas.

The linear polarisation of the UV light is usually vertical (*i.e.*, with the electric vector parallel to the vertical TOF axis – see Fig. 1), as in the measurements of Fig. 2. With horizontal polarisation (*i.e.*, where the electric vector is orthogonal to the TOF axis), the amplitude of feature **B** is undiminished and those of features **C** and **D** are reduced by a factor of ~3; by contrast, the O^+ REMPI signals in feature **A** vanish, showing that the spatial distribution of O^+, formed by photodissociation of O_2^+ ($A\ ^2\Pi_u$) as in Eq. (4), is highly anisotropic.

It should be noted that most of the KER in the processes that generate O_2^+, as in Eqs (1)–(3), is taken up by photoelectrons, but that the 0.88-eV KER in Eq. (4) is shared equally

between O (^3P) atoms and O^+ (^2D) ions. With vertical UV polarisation, the anisotropically distributed O^+ ions propagate initially in either forward or backward directions along the TOF axis; all of the backward-ejected O^+ ions are likely to hit the repeller plate when V_1 is low (< 4.5 V) and none reach the MCP detector at any V_1 with the orthogonal horizontal polarisation.

UV-TPE TOF experiments have also been performed with the UV pulse energy (proportional to I_{UV}) attenuated by a factor of 1.9. The TOF signals for features **C** and **D** of Fig. 2 are attenuated by a factor of exactly $(1.9)^3$, consistent with (2 + 1) REMPI processes for O_2^+ below optical saturation. Likewise, the O^+ TOF signals, as in feature **A** of Fig. 2, are attenuated by a factor of $(1.9)^4$, which is consistent with unsaturated (2 + 1 + 1) REMPI. On the other hand, the TOF-signal amplitudes for the V_1-insensitive feature **B** of Fig. 2 vary as $(1.9)^2$, which corresponds to UV TPE to the O_2 $5d\pi$ $^1\Sigma_g^+$ Rydberg state and UV-independent ionisation.

The irregular feature **B** of Fig. 2 is the only signal observed in our TOF scans when the potential difference V_1 in the photoionisation zone **1** is zero. With an acceleration voltage V_2 = 41.5 V, this peak appears at a constant TOF delay of 9.78 ± 0.03 μs. With (V_1 + V_2) fixed at 44.0 V and over a range of V_2 from 38.5 V to 43.5 V, the measured (V_1, V_2)-dependence of the TOF delay for feature **B** is approximated by (14.75 – 0.12 V_2). Features **A** and **B** are both attributed to formation of O^+ ions after TPE of O_2 ($5d\pi$ $^1\Sigma_g^+$) molecules. However, the V_1-insensitivity and $(I_{UV})^2$-dependence of the latter indicate that O^+ ions are formed outside the UV-irradiation zone **1** (*i.e.*, not before they reach the extraction grid EG, as depicted in Fig. 1).

As indicated in Secs 3.1 and 3.3, spontaneous predissociation of O_2 ($5d\pi$ $^1\Sigma_g^+$) Rydberg molecules is a likely mechanism. We consider five possible schemes, as follows:

$$O_2\ (5d\pi\ ^1\Sigma_g^+ / {}^1\Pi_g) \rightarrow O\ (^1D) + O\ (^1S) + (\text{KER} = 0.52\ \text{eV}), \quad \text{(A1)}$$

$$O_2\ (5d\pi\ ^1\Sigma_g^+ / {}^3\Pi_g) \rightarrow O\ (^3P) + O\ (^1S) + (\text{KER} = 2.40\ \text{eV}), \quad \text{(A2)}$$

$$O_2\ (5d\pi\ ^1\Sigma_g^+ / {}^1\Pi_g) \rightarrow O\ (^1D) + O\ (^1D) + (\text{KER} = 2.75\ \text{eV}), \quad \text{(A3)}$$

$$O_2\ (5d\pi\ ^1\Sigma_g^+ / {}^3\Pi_g) \rightarrow O\ (^3P) + O\ (^1D) + (\text{KER} = 4.71\ \text{eV}), \quad \text{(A4)}$$

$$O_2\ (5d\pi\ ^1\Sigma_g^+ / {}^1\Pi_g \text{ or } {}^3\Pi_g) \rightarrow O\ (^3P) + O\ (^3P) + (\text{KER} = 6.68\ \text{eV}), \quad \text{(A5)}$$

where possible iso-energetic predissociative perturbations of the TPE-generated O_2 ($5d\pi$ $^1\Sigma_g^+$) Rydberg manifold, by overlapping repulsive potential curves for $^1\Pi_g$ or $^3\Pi_g$ valence states (as discussed in Sec. 3.3), are indicated after the "/" symbol. KER values are derived by subtracting relevant photodissociation energies [28] from the 11.795-eV TPE energy. Each of the resulting O atoms takes half of the KER (*i.e.*, 0.26, 1.20, 1.37, 2.35 and 3.34 eV, respectively). It is apparent that (consistent with our UV-polarisation measurements) they have an isotropic

spatial distribution. The properties of feature **B** (in Fig. 2 and elsewhere) indicate that O atoms are not converted to O^+ ions until they have left zone **1** (such that signals recorded by the MCP arise from an ionisation process that is both UV- and V_1-independent). Moreover, TOF plots such as those in Fig. 2 show that ionisation is synchronous with TPE by each laser pulse.

In order for the UV TPE spectral linewidth of feature **B** to match that recorded for feature **C** (as shown in Figs 3 and 4), the relevant predissociation process observed is expected to be rapid, with $\tau < 10$ ps. As discussed in Sec. 3.3, such a predissociation efficiency is likely to be enhanced by spin-orbit coupling [10,11,34]. This would be most readily realised *via* perturbations from a repulsive $^3\Pi_g$ valence state, as envisaged in Eqs (A2), (A4) or (A5).

On this basis, we have considered possible mechanisms for feature **B** in which some of the predissociated O atoms propagate directly along the TOF axis in zone **1** over a distance of ~11 mm before interacting momentarily with the extraction-grid electrode EG where they form O^+ ions. These ions are then accelerated in zone **2**, with potential difference V_2 over distance $d_2 = 25$ mm, until they drift in the field-free zone **3** over $d_3 = 90$ mm to the MCP.

In our simplest kinematic calculations, the interactions at EG that convert O to O^+ are assumed to be instantaneous, with electrons taking away virtually all of the kinetic energy and leaving O^+ initially at rest. It is then estimated that, for $38.5\ \text{V} \leq V_2 \leq 43.5\ \text{V}$, a total KER of ~1.5–1.7 eV is needed to achieve close agreement between observed and predicted values of t_{TOF}. This hypothetical KER falls in between those of Eq. (A1), which is not directly amenable to spin-orbit coupling and overestimates the flight time t_{TOF} by ~2.5–2.8 μs, and Eq. (A2), which can enhance predissociation by spin-orbit coupling and undererestimates t_{TOF} by ~0.7_5–0.9_5 μs. Spin-orbit coupling is also enabled by the more exothermic schemes in Eqs (A4) and (A5) but they underestimate t_{TOF} by ~1.0_5–1.2_5 μs and ~1.4–1.6 μs, respectively. It therefore seems that the presumed ionisation mechanism for O atoms in the vicinity of EG is not instantaneous and is still open to speculation. Possible momentum transfers from the gas jet or from O to O^+ at EG do not adequately explain these discrepancies, so that the formation of O^+ ions at the surface of EG (before they are accelerated in zone **2** and drift to the MCP) remains poorly understood.

Fig. 2(c) shows that, when $V_1 \geq 4.5$ V, another peak, labelled **B'**, branches out from peak **B** towards lower TOF values. In fact, peak **B'** has a non-zero V_1-dependence and is not a satellite of peak **B**. Our kinematic calculations attribute it to backward-ejected O^+ ions formed by (2 + 1 + 1) REMPI as in the context of Eqs (2) and (4). When $V_1 < 4.5$ V, these backward-ejected O^+ ions are removed by impact with the repeller plate. However, higher values of V_1

cause the anisotropically distributed O^+ ions that initially propagate backwards to be reflected towards the MCP before they reach the repeller plate. We estimate that, for V_1 = 5.0 V and 5.5 V, these O^+ (^2D) ions (with an initial backward kinetic energy of 0.44 eV) are decelerated to rest within distances of 1.08 mm and 0.98 mm, respectively, after which they are accelerated with total flight times t_{TOF} of 9.55 μs and 9.40 μs, agreeing well with our TOF observations for peak **B'**.

Acknowledgments

The vacuum chambers and TOF detection system, as first used in [25], were supplied by the late Professor Ed Eyler. We thank Dr Colin Western for guidance with regard to his PGOPHER program [32] and Dr Matt Sellars for supportive loans of apparatus. This work was supported by the Australian Research Council [Discovery Project number DP110101002], as well as by our respective universities.

References

[1] Flory PJ. Predissociation of the oxygen molecule. J Chem Phys 1936; 4: 23–7. https://doi.org/10.1063/1.1749741 .

[2] Carroll PK. Predissociation in the Schumann-Runge bands of oxygen. Astrophys J 1959; 129: 794–800. https://doi.org/10.1086/146675 .

[3] Dooley PM, Lewis BR, Gibson, ST, Baldwin KGH, Cosby PC, Price JL, Copeland RA, Slanger TG, Thorne AP, Murray JE, Yoshino K. A comparative high-resolution study of predissociation linewidths in the Schumann-Runge bands of O_2. J Chem Phys 1998; 109(10): 3856–67. https://doi.org/10.1063/1.476986 .

[4] Tong GSM, Cheung AS-C, Jamieson M, Predicted predissociation linewidths in the Schumann-Runge bands of O_2 compared with recent high-resolution measurements. J Chem Phys 2001; 114(18): 7969–75. https://doi.org/10.1063/1.1361255 .

[5] Lewis BR, Gibson, ST, Baldwin KGH, Dooley PM, Waring K. Comparative very-high-resolution VUV spectroscopy: laser spectroscopy of O_2. Surface Rev Lett 2002; 9(1): 31–8. https://doi.org/10.1142/S0218625X02001690 .

[6] Dooley PM, Lewis BR, Waring K, Gibson ST, Baldwin KGH. Fine-structure-resolved collisional broadening in the Schumann-Runge bands of O_2. J Quant Spectrosc Radiat Transf 1997; 58(1): 93–100. https://doi.org/10.1016/S0022-4073(97)00024-1 .

[7] Lewis BR, Dooley PM, England JP, Gibson ST, Baldwin KGH, Torop LW. Non-Lorentzian line shapes for interfering rotational resonances in the predissociation of O_2. Phys Rev A 1997; 55(6): 4164–7. https://doi.org/10.1103/PhysRevA.55.4164 .

[8] Lewis BR, Gibson ST, Torop LW, McCoy DG. Quantum interference in the Schumann-Runge bands of molecular oxygen. Geophys Res Lett 1998; 25(13): 2457–60. https://doi.org/10.1029/98GL51783 .

[9] Kono M, Lewis BR, Baldwin KGH, Gibson ST. Experimental verification of line- and band-shape asymmetry in the Schumann-Runge system of O_2. J Chem Phys 2003; 118(24): 10924–8. https://doi.org/10.1063/1.1574512 .

[10] Morrill JS, Ginter ML, Lewis BR, Gibson ST. The $(X\,^2\Pi_g)\ ns\sigma_g\ ^{1,3}\Pi_g$ Rydberg states of O_2: Spectra, structures, and interactions. J Chem Phys 1999: 111(1): 173–85. https://doi.org/10.1063/1.479264 .

[11] Lewis BR, Gibson ST, Morrill JS, Ginter ML. Perturbations in the $3s\sigma_g\ ^{1,3}\Pi_g$ Rydberg states of O_2: Bound–bound interactions with the second $^1\Pi_g$ and $^1\Delta_g$ valence states. J Chem Phys 1999; 111(1): 186–97. https://doi.org/10.1063/1.479265 .

[12] Gilchrist AJ, Ritchie GAD. Predissociation dynamics of the $C\,^3\Pi_g$ Rydberg state of molecular oxygen. J Chem Phys 2013; 138: 104320 (10 pages). https://doi.org/10.1063/1.4794694 .

[13] Gilchrist AJ, Ritchie GAD. Atomic orientation following predissociation of the $C\,^3\Pi_g$ Rydberg state of molecular oxygen. J Chem Phys 2013; 138: 214307 (8 pages). https://doi.org/10.1063/1.4807761 .

[14] Buijsse B, van der Zande WJ, Eppink ATJB, Parker DH, Lewis BR, Gibson ST. Angular distributions for photodissociation of O_2 in the Herzberg continuum. J Chem Phys 1998; 108(17): 7229–43. https://doi.org/10.1063/1.476141 .

[15] Alexander AJ, Kim ZH, Zare RN. Photodissociation of O_2 *via* the Herzberg continuum: Measurements of O-atom alignment and orientation. J Chem Phys 2003; 118(23): 10566–74. https://doi.org/10.1063/1.1574511 .

[16] Pratt ST, Dehmer JL, Dehmer PM. Two-photon spectroscopy of Rydberg states of molecular oxygen. J Chem Phys 1990; 93(5): 3072–84. https://doi.org/10.1063/1.458841 .

[17] Park H, Miller PJ, Chupka WA, Colson SD. Production of vibrationally state-selected O_2^+ via newly discovered 4*s*–3*d* and 5*s*–4*d* Rydberg states of O_2. J Chem Phys 1988; 89(6): 3919–21. https://doi.org/10.1063/1.454867 .

[18] Park H, Miller PJ, Chupka WA, Colson SD. Multiphoton optical and photoelectron spectroscopy of 4*s*–3*d* and 5*s*–4*d* Rydberg complexes of O_2. J Chem Phys 1988; 89(11): 6676–86. https://doi.org/10.1063/1.455340 .

[19] Ogorzalek-Loo R, Marinelli WJ, Houston PL, Arepalli S, Wiesenfeld JR, Field RW. Multiphoton ionization of O_2 $X\,^3\Sigma_g^-$, $a\,^1\Delta_g$, and $b\,^1\Sigma_g^+$ via the two-photon resonant $ns\sigma_g$, $nd\sigma_g$, and $nd\pi_g$ Rydberg levels. J Chem Phys 1989; 91(9): 5185–200. https://doi.org/10.1063/1.457589 .

[20] Kono M, He Y, Baldwin KGH, Orr BJ. Sub-Doppler two-photon spectroscopy of 33 Rydberg levels in atomic xenon excited at 205-213 nm: diverse isotopic and hyperfine structure. J Phys B 2013; 46(3): 035401 (16 pages). https://doi.org/10.1088/0953-4075/46/3/035401 .

[21] Kono M, He Y, Baldwin KGH, Orr BJ. Sub-Doppler two-photon-excitation Rydberg spectroscopy of atomic xenon: mass-selective studies of isotopic and hyperfine structure. J Phys B 2016; 49(6): 065002 (15 pages). https://doi.org/10.1088/0953-4075/49/6/065002 .

[22] He Y, Kono M, White RT, Sellars MJ, Baldwin KGH, Orr BJ. Coherent heterodyne-assisted pulsed spectroscopy: Sub-Doppler two-photon spectra of krypton, characterizing a tunable nonlinear-optical ultraviolet light source. Appl Phys B 2010; 99(4): 609–12. https://doi.org/10.1007/s00340-010-3982-1 .

[23] Kono M, Baldwin KGH, HeY, White RT, Orr BJ. Heterodyne-assisted pulsed spectroscopy with a nearly Fourier-transform limited, injection-seeded optical parametric oscillator. Opt Lett 2005; 30(24): 3413–5. https://doi.org/10.1364/OL.30.003413 .

[24] Kono M, Baldwin KGH, HeY, White RT, Orr BJ. CHAPS: a new precision laser-spectroscopic technique. J Opt Soc Am B 2006; 23(6): 1181–9. https://doi.org/10.1364/JOSAB.23.001181 .

[25] Bergeson SD, Baldwin KGH, Lucatorto TB, McIlrath TJ, Cheng CH, Eyler EE. Doppler-free two-photon spectroscopy in the vacuum ultraviolet: helium $1\,^1S - 2\,^1S$ transition. J Opt Soc Am B 2000; 17(9): 1599–606. https://doi.org/10.1364/JOSAB.17.001599 .

[26] Wiley WC, McLaren IH. Time-of-flight mass spectrometer with improved resolution. Rev Sci Instrum 1955; 26(12): 1150–7. https://doi.org/10.1063/1.1715212 .

[27] Huber KP, Herzberg G. Molecular Spectra and Molecular Structure IV. Constants of Diatomic Molecules. New York: Van Nostrand; 1979, p. 504–5. ISBN 0-442-23394-9 (v. 4). https://webbook.nist.gov/cgi/cbook.cgi?Formula=O2&Units=SI&cDI=on [Accessed 30 September 2019]..

[28] Burkholder JB, Sander SP, Abbatt J, Barker JR, Huie RE, Kolb CE *et al*. Chemical Kinetics and Photochemical Data for Use in Atmospheric Studies, Evaluation No. 18 (JPL Publication 15-10). Pasadena: Jet Propulsion Laboratory; 2015; p. 4-11. http://jpldataeval.jpl.nasa.gov [Accessed 30 September 2019].

[29] Kramida A, Ralchenko Y, Reader J, Saloman EB, Olsen K. Atomic Spectra Database (version 5.7). Gaithersburg: National Institute of Standards and Technology; 2018. https://dx.doi.org/10.18434/T4W30F .

[30] Herzberg G. Molecular Spectra and Molecular Structure I. Spectra of Diatomic Molecules. 2nd ed. New York: Van Nostrand; 1950; p. 221. ISBN 0-442-23394-9 (v. 1).

[31] Fano U. Effects of configuration interaction on intensities and phase shifts. Phys Rev 1961; 124(6): 1866–78. https://doi.org/10.1103/PhysRev.124.1866 .

[32] Western CM. PGOPHER: A program for simulating rotational, vibrational and electronic spectra. J Quant Spectrosc Radiat Transf 1997; 186: 221–42. https://doi.org/10.1016/j.jqsrt.2016.04.010 .

[33] Mahon R, Tomkins F. Frequency up-conversion to the VUV in Hg vapor. IEEE J Quant Electron 1982; QE-18(5): 913–20. https://doi.org/10.1109/JQE.1982.1071625 .

[34] Lefebvre-Brion H, Field RW. Perturbations in the Spectra of Diatomic Molecules Orlando: Academic; 1986. ISBN 0-12-44690-5.

[35] Miroshnichenko AE, Flach S, Kivshar YS. Fano resonances in nanoscale structures. Rev Mod Phys 2010; 82(3): 2257–98. https://link.aps.org/doi/10.1103/RevModPhys.82.2257 .

[36] Mezei JZs, Schneider IF, Jungen Ch. Multichannel quantum defect theory of photo-dissociation in H_2. EPJ Web of Conferences 2015; 04005 (10 pages). https://doi.org/10.1051/epjconf/20158404005 .

[37] Parker, DH. Laser Photochemistry of molecular oxygen. Acc Chem Res 2000; 33(8): 563–71. https://doi.org/10.1021/ar980012d .

[38] Parker, DH, Eppink, ATJB. Photoelectron and photofragment velocity map imaging of state-selected molecular oxygen dissociation/ionization dynamics. J Chem Phys 1997; 107(7): 2357–62. https://doi.org/10.1063/1.474624 .

[39] Gibson, ST, Lewis BR, Baldwin KGH, Carver JH. Rotational features in the fluorescence excitation spectrum of $O(^1D_2)$ from vacuum ultraviolet laser photodissociation of O_2. J Chem Phys 1990; 94(2): 1060–8. https://doi.org/10.1063/1.460062 .